Inside the Bondi radius of M87

H. R. Russell[1,2]∗, A. C. Fabian[1], B. R. McNamara[2,3,4] and A. E. Broderick[2,3]

[1] Institute of Astronomy, Madingley Road, Cambridge CB3 0HA
[2] Department of Physics and Astronomy, University of Waterloo, Waterloo, ON N2L 3G1, Canada
[3] Perimeter Institute for Theoretical Physics, Waterloo, Canada
[4] Harvard-Smithsonian Center for Astrophysics, 60 Garden Street, Cambridge, MA 02138, USA

9 June 2015

ABSTRACT

Chandra X-ray observations of the nearby brightest cluster galaxy M87 resolve the hot gas structure across the Bondi accretion radius of the central supermassive black hole, a measurement possible in only a handful of systems but complicated by the bright nucleus and jet emission. By stacking only short frame-time observations to limit pileup, and after subtracting the nuclear PSF, we analysed the X-ray gas properties within the Bondi radius at $0.12 - 0.22$ kpc ($1.5 - 2.8$ arcsec), depending on the black hole mass. Within 2 kpc radius, we detect two significant temperature components, which are consistent with constant values of 2 keV and 0.9 keV down to 0.15 kpc radius. No evidence was found for the expected temperature increase within ~ 0.25 kpc due to the influence of the SMBH. Within the Bondi radius, the density profile is consistent with $\rho \propto r^{-1}$. The lack of a temperature increase inside the Bondi radius suggests that the hot gas structure is not dictated by the SMBH's potential and, together with the shallow density profile, shows that the classical Bondi rate may not reflect the accretion rate onto the SMBH. If this density profile extends in towards the SMBH, the mass accretion rate onto the SMBH could be at least two orders of magnitude less than the Bondi rate, which agrees with Faraday rotation measurements for M87. We discuss the evidence for outflow from the hot gas and the cold gas disk and for cold feedback, where gas cooling rapidly from the hot atmosphere could feed the cirumnuclear disk and fuel the SMBH. At 0.2 kpc radius, the cooler X-ray temperature component represents $\sim 20\%$ of the total X-ray gas mass and, by losing angular momentum to the hot gas component, could provide a fuel source of cold clouds within the Bondi radius.

Key words: X-rays: galaxies: clusters — galaxies: clusters: M87 — intergalactic medium

1 INTRODUCTION

Accretion onto the supermassive black hole (SMBH) at the centre of the giant elliptical galaxy M87 is powering relativistic jet activity that heats the surrounding hot cluster atmosphere and stifles galaxy growth (Forman et al. 2005, 2007). Deep *Chandra* X-ray observations of the intracluster medium have found large cavities filled with radio emission where the X-ray gas has been displaced by the expansion of the jet (Bohringer et al. 1995; Bicknell & Begelman 1996; Young et al. 2002; Forman et al. 2005, 2007). This energy input is likely suppressing the rapid cooling of the dense, low temperature X-ray gas at the centre of the cluster, which would otherwise flood the brightest cluster galaxy (BCG) with cold molecular gas and ensuing star formation (eg. Peterson & Fabian 2006). In general, this feedback from the central AGN is thought to be the essential mechanism in models of galaxy formation that truncates galaxy growth by restricting gas cooling and star formation (Croton et al. 2006; Bower et al. 2006; Hopkins et al. 2006).

The central AGN is located in the densest region of the cluster's hot atmosphere and therefore classical Bondi accretion of the hot gas is often considered as a fuelling mechanism for feedback (Bondi 1952; Baganoff et al. 2003; Di Matteo et al. 2003). The gas will be accreted by the SMBH if it lies within the Bondi radius, where the gravitational potential of the SMBH dominates the thermal energy of the hot atmosphere. The Bondi radius is given by $r_{\rm B} = 2GM_{\rm BH}/c_s^2$, where $M_{\rm BH}$ is the mass of the black hole and c_s is the sound speed of the hot gas. Using *Chandra* observations of M87, Di Matteo et al. (2003) found that the Bondi accretion rate is able to provide a sufficient supply of fuel to power the AGN. However, Bondi accretion of the hot gas may be insufficient to fuel the most powerful radio jet outbursts (eg. Rafferty et al. 2006; McNamara et al. 2011). Cold gas accretion from circumnuclear disks of atomic and molecular gas may be required to supplement the fuel supply (eg. Pizzolato & Soker 2005).

For accretion at the Bondi rate, the radiative output from the nucleus in M87 is orders of magnitude below the expectation from standard thin disk accretion (Fabian & Canizares 1988; Fabian & Rees 1995; Di Matteo et al. 2000). The black hole at the centre

∗ E-mail: hrr27@ast.cam.ac.uk

© 0000 RAS

Table 1. Details of the *Chandra* observations used for this analysis and best-fit nuclear spectral model parameters.

Obs. ID	Date	Exposure (ks)	Frame time (s)	$n_{\rm H}$ (10^{22} cm^{-2})	Γ	Flux (2 − 10 keV) (10^{-12} erg cm^{-2} s^{-1})
352	29/07/2000	29.4	3.2	-	-	-
1808	30/07/2000	12.8	0.4	0.08 ± 0.01	2.37 ± 0.07	0.70 ± 0.04
11513	13/04/2010	4.7	0.4	0.06 ± 0.02	2.35 ± 0.08	$1.42^{+0.10}_{-0.09}$
11514	15/04/2010	4.5	0.4	0.05 ± 0.02	2.15 ± 0.09	1.4 ± 0.1
11515	17/04/2010	4.7	0.4	0.04 ± 0.02	2.21 ± 0.08	1.6 ± 0.1
11516	20/04/2010	4.7	0.4	0.02 ± 0.02	2.02 ± 0.08	1.7 ± 0.1
11517	05/05/2010	4.7	0.4	0.08 ± 0.02	2.34 ± 0.08	$1.54^{+0.10}_{-0.09}$
11518	09/05/2010	4.0	0.4	0.06 ± 0.02	2.3 ± 0.1	$1.17^{+0.10}_{-0.09}$
11519	11/05/2010	4.7	0.4	0.08 ± 0.02	2.4 ± 0.1	1.02 ± 0.08
11520	14/05/2010	4.6	0.4	0.11 ± 0.02	2.5 ± 0.1	$1.01^{+0.08}_{-0.07}$
13964	05/12/2011	4.5	0.4	0.07 ± 0.02	$2.31^{+0.10}_{-0.09}$	$1.17^{+0.09}_{-0.08}$
13965	25/02/2012	4.6	0.4	0.04 ± 0.02	2.11 ± 0.09	1.5 ± 0.1
14973	12/03/2013	4.4	0.4	0.05 ± 0.02	2.3 ± 0.1	1.18 ± 0.09
14974	12/12/2012	4.6	0.4	0.05 ± 0.03	2.2 ± 0.1	1.17 ± 0.09
Stack		54.7	0.4	0.057 ± 0.006	2.25 ± 0.03	1.30 ± 0.03

of the Milky Way, Sgr A*, is a good example of a low luminosity AGN with a radiative output several orders of magnitude below that implied by the Bondi accretion rate and the standard 10% radiative efficiency (eg. Baganoff et al. 2003; Genzel et al. 2010). This observed radiative inefficiency of the accretion disk is consistent with an advection-dominated accretion flow where the gas is unable to radiate the gravitational potential energy locally and the trapped energy is instead advected inward (Ichimaru 1977; Rees et al. 1982; Narayan & Yi 1994; Narayan & McClintock 2008). Alternatively, the mass inflow at the Bondi radius may not reach the event horizon of the SMBH but is instead ejected from the black hole's sphere of influence (ADIOS; Blandford & Begelman 1999, 2004) or circulates in convective eddies (CDAF; Narayan et al. 2000; Quataert & Gruzinov 2000).

It has proven difficult to distinguish between these possibilities, or indeed to determine the fuelling mechanism of the AGN, because it is only possible to resolve the hot gas inside the Bondi radius in a handful of systems. Deep *Chandra* observations of two of the best targets, Sgr A* and NGC3115 (Baganoff et al. 2003; Wong et al. 2011), are consistent with flat density profiles with $\rho \propto r^{-1}$ inside the Bondi radius (Wang et al. 2013; Wong et al. 2014). This is consistent with recent numerical simulations which show outflows in the form of winds off the accretion flow preventing all but a fraction of the Bondi rate from reaching the SMBH (eg. Yuan et al. 2012; Li et al. 2013). However, whilst such a low mass accretion rate is adequate for these quiescent systems, it is insufficient to fuel powerful radio-jet outbursts without requiring efficiencies much greater than 100% (Nemmen & Tchekhovskoy 2014). Such high efficiencies are theoretically achievable if the black hole spin energy can be extracted (Tchekhovskoy et al. 2011; Tchekhovskoy & McKinney 2012; McKinney et al. 2012) but alternatively, the inflow rate may be significantly increased by cold gas accretion, which compensates for the outflowing mass (Pizzolato & Soker 2005; Gaspari et al. 2013).

At a distance of only ~ 16 Mpc, M87 at the centre of the Virgo cluster is one of few systems for which *Chandra* can resolve the Bondi radius at ~ 2 arcsec (~ 0.15 kpc; Di Matteo et al. 2003; Garcia et al. 2010). Hosting a powerful radio jet outburst and a circumnuclear gas disk (Ford et al. 1994; Harms et al. 1994; Macchetto et al. 1997), M87 provides an excellent comparison system to NGC3115 and Sgr A* to determine the properties of the putative

accretion flow. However, the bright nuclear point source and jet knots make it challenging to extract the properties of the underlying cluster gas across the Bondi radius. Early *Chandra* observations of M87 in 2000 showed that the bright nucleus and jet emission would not be piled up in a 0.4 s frame time observation (Wilson & Yang 2002; Perlman & Wilson 2005). Di Matteo et al. (2003) used this short 12.8 ks observation to determine the gas properties using single temperature spectral models in to 2 arcsec radius. In 2005, major flaring of the jet knot HST-1, located only 0.85 arcsec from the nucleus, then resulted in strong pileup even in short frame-time observations (Harris et al. 2006) and prevented follow up studies. However, HST-1 has slowly declined in brightness since the peak in 2005 and Harris et al. (2011) found that by 2010 the intensity had dropped to the level observed in 2000.

Here we stack twelve 5 ks monitoring observations of M87 taken since April 2010 (PI Harris) and subtract the bright nuclear emission to determine the density profile inside the Bondi radius and study the temperature structure on these scales. Section 2 describes the observations, data reduction and subtraction of the nuclear emission. In section 3, we determine the temperature and density structure within the Bondi radius and calculate the cooling and dynamical time profiles. We discuss accretion of the hot gas atmosphere by the SMBH and the evidence for hot and cold gas outflows in section 4 before presenting our conclusions in section 5. We assume a distance to M87 of 16.1 Mpc (Tonry et al. 2001) to be consistent with earlier analyses of the *Chandra* datasets. This gives a linear scale of 0.078 kpc arcsec^{-1} and $\sim 2-5 \times 10^5$ gravitational radii per arcsec, depending on the black hole mass (section 3.4). All errors are 1σ unless otherwise noted.

2   *CHANDRA* DATA ANALYSIS

The centre of M87 has been observed regularly with *Chandra* since 2002 to monitor jet activity, understand the emission mechanism and determine the site of the TeV flaring (Harris et al. 2003, 2006, 2009, 2011). For this study of the central cluster gas properties, we have selected all archival *Chandra* observations of M87 taken since the intensity of HST-1 dropped back to its 2000 level and after the TeV flaring event in early April 2010 (Ong & Mariotti 2010; Harris et al. 2011). These ACIS-S datasets were also compared with two of
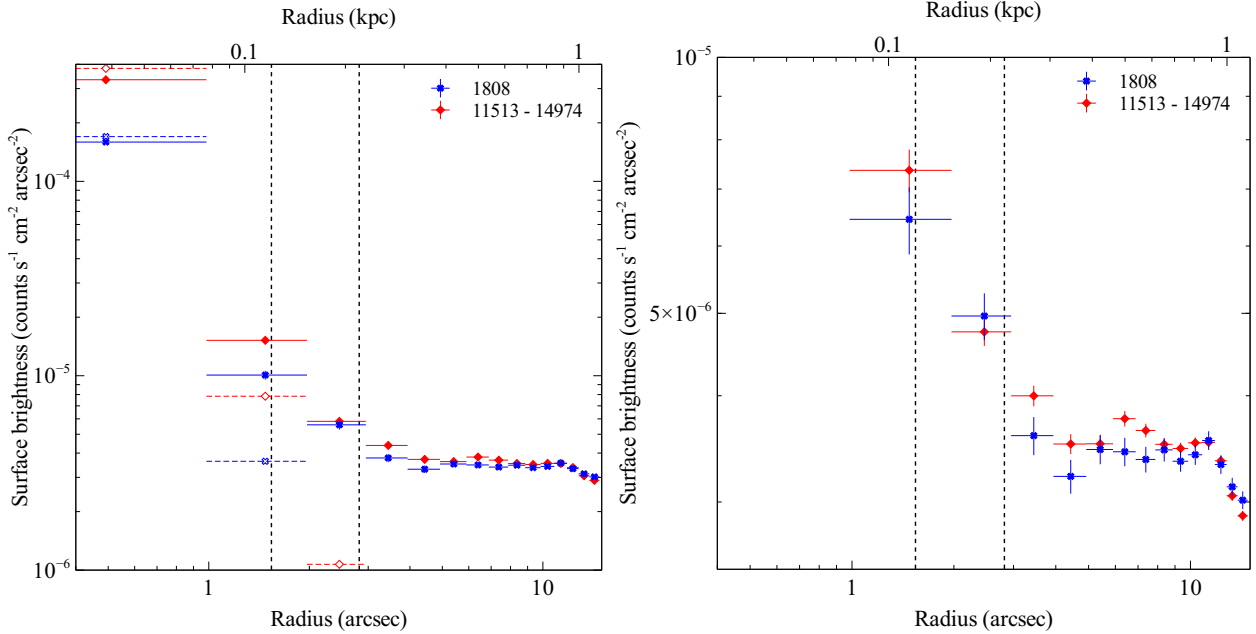
Figure 1. Left: Background-subtracted surface brightness profiles in the energy range $0.5 - 7.0$ keV for obs. ID 1808 and the summed obs. IDs 11513 to 14974. The ChaRT simulations of the nuclear flux for each observation are shown by the open symbols. Right: Same as left but with the nuclear flux subtracted from each profile. The radial range for the Bondi radius is shown by the vertical dashed lines.

the ACIS-S observations taken in 2000 to test the subtraction of the nuclear emission (obs. ID 1808) and determine the gas properties to large radii for the deprojection analysis (obs. ID 352). We have not included the short, < 1 ks, exploratory observation, which was taken to determine the nuclear count rate and therefore the frame time suitable for the later observations (obs. ID 351).

All datasets were analysed with CIAO version 4.6 and CALDB version 4.6.2 supplied by the *Chandra* X-ray Center (Fruscione et al. 2006). Level 1 event files were reprocessed with the latest gain and charge transfer inefficiency correction applied and then filtered to remove cosmic ray events. Background light curves were extracted from regions free of point sources and used to remove periods affected by flares from the event files. The combined dataset was also examined for any periods with high background count rates. No flares were found in the short frame-time observations and only two short flares occurred during obs. ID 352. The final cleaned exposure times are given in Table 1.

The cluster emission from M87 extends across the entire *Chandra* field of view, therefore blank-sky background observations were used to subtract the background from images and spectra. The appropriate blank-sky background dataset was processed identically to the event file, reprojected to the same sky position and normalized so that the count rate matched that of the event file for the $9.5 - 12$ keV energy band. Point sources were identified using a hard band ($3 - 5$ keV) image for each observation and excluded from the analysis. The shallow datasets from 2010 to 2013 were also reprojected to a common position and combined to ensure that no faint point sources were missed. This method identified and excluded all point sources found by Jordán et al. (2004). The remaining contaminating flux from unresolved low mass X-ray binaries and the stellar population (cataclysmic variables and coronally active binaries) is insignificant at only $\sim 1\%$ of the total emission in M87 in the $0.5 - 2$ keV energy band (Revnivtsev et al. 2008). The cluster emission dominates at energies below 10 keV and the point

source emission only becomes significant at higher energies. The emission from the jet was also carefully excluded.

2.1 Subtracting the nuclear PSF

Within 1 arcsec, the nuclear point source is more than an order of magnitude brighter than the cluster emission. Although the cluster emission dominates beyond ~ 3 arcsec, the Bondi sphere is located within this region. It was therefore necessary to accurately model and subtract the nuclear point spread function (PSF) to determine the gas properties across the Bondi radius. This analysis is described in detail in the appendix, including an evaluation of the low-level pileup, the nuclear spectral model and simulations of the PSF. In summary, following Russell et al. (2010) and Siemiginowska et al. (2010), we used the best-fit power law model for the nuclear spectrum (Table 1) and the *Chandra* ray-tracer (ChaRT; Carter et al. 2003) to simulate the nuclear PSF (photons scattered by the *Chandra* mirrors). This simulation was then projected onto the ACIS detector with MARX and used to subtract the PSF contamination from the cluster emission at each radius within the cluster core. We assume that all emission within 1 arcsec is from the AGN. However the gas emission is likely to be $\sim 5\%$ of the total, depending on the slope of the gas density profile (section A2).

The simulation was tested by comparing the PSF-subtracted surface brightness profiles for two separate epochs (obs. ID 1808 and the stacked 11513 to 14974 observations). Fig. 1 (left) shows the total emission profiles and the predicted contribution of the PSF, which has varied significantly in flux between the two epochs. Fig. 1 (right) shows the subtracted profiles, which incorporate the uncertainty on the nuclear flux (Table 1). The flux of the PSF simulation was increased to compensate for the reduction due to mild pileup within 1 arcsec, which causes an oversubtraction of the AGN emission in this region (section A3). The subtracted profiles agree within the errors showing that the majority of the variable nuclear

emission has been removed and only the cluster emission remains. Although the ChaRT/MARX simulation is not expected to provide an exact prediction of the PSF to large radii (eg. Gaetz & Jerius 2005), the nuclear flux is only significant to ~ 3 arcsec radius and the excellent agreement between the subtracted profiles in Fig. 1 (right) suggests this method is sufficiently accurate for our analysis.

The combined effect of the minor inaccuracies in the nuclear PSF subtraction due to the cluster contamination, mild pileup, nuclear spectral model and effective area reduction (section A3) was determined by comparing the subtracted profiles from these different epochs. In Fig. 1, the cluster surface brightness in the $1 - 2$ arcsec radial bin, where the uncertainty due to the PSF subtraction is largest, agrees within the errors. This suggests that the difference in flux between the two epochs is less than $\sim 15\%$. The nuclear PSF flux is significantly lower in obs. ID 1808 therefore it is more likely that the PSF contribution has been underestimated in the summed observations. To be conservative, we have estimated the impact on the measured gas properties if the PSF flux is systematically higher by 20%. Variation in the photon index by ± 0.2 and absorption by $\pm 0.05 \times 10^{22}$ cm^{-2} produced uncertainties in the measured temperature and density values less than the statistical error and therefore is not significant in comparison to the uncertainty in the nuclear flux.

2.2 Spectral analysis and deprojection

Fig. 2 (left) shows the complex cavity structures and bright blobs and filaments of cool gas located at the centre of M87. These gas structures have been studied in detail by Young et al. (2002), Forman et al. (2005), Forman et al. (2007), Million et al. (2010) and Werner et al. (2010). Clear depressions are observed in the X-ray emission to the west of the nucleus beyond the jet, immediately south-east of the nucleus and to the south and east of that (~ 20 arcsec from the nucleus). These depressions are cavities carved out by the radio jet and buoyantly rising through the surrounding atmosphere (eg. Churazov et al. 2000; McNamara et al. 2000; Fabian et al. 2000; McNamara & Nulsen 2007). Fig. 2 (right) shows the angular variation in surface brightness around the nucleus. The inner cavity to the south-east can be clearly seen in the $140 - 234°$ sector. This cavity is surrounded by a rim of cool gas that is visible as a bright ridge of emission. The X-ray surface brightness to the north and south of the nucleus is clumpy and several point sources are visible, which were excluded from the profiles. However, there is less angular variation in the surface brightness inside ~ 4 arcsec radius. We have therefore proceeded with azimuthally-averaged density and temperature profiles.

Spectra were extracted from circular annuli extending to a radius of 14 arcsec centred on the nucleus for obs. IDs 11513 to 14974. The radial range from these observations was limited by the subarray selection and therefore spectra were also extracted from obs. ID 352 to extend the radial profiles to ~ 300 arcsec. Although there has been a significant decrease in the effective area at low energies between these observations due to the contaminant build up (Marshall et al. 2004), the surface brightness profiles are consistent in the region of overlap (section A3). Background spectra were generated from the blank sky backgrounds for each source spectrum and appropriate responses and ancillary responses were produced. The spectra were restricted to the energy range $0.5 - 7$ keV and grouped with a minimum of 25 counts per energy bin. For obs. IDs 11513 to 14974, the source was located at a similar position on the same chip and therefore the responses were comparable. We

summed together the spectra and background spectra for each annulus and averaged the response files with a weighting determined by the fraction of the total counts in each observation. The summed spectra contained a minimum of 3000 counts in each of the narrowest 2 arcsec radial bins and over $40,000$ in the broader radial bins.

The summed spectra covering radii out to 14 arcsec and the obs. ID 352 spectra from 14 to 300 arcsec radius were deprojected with the model-independent spectral deprojection routine DSDE-PROJ (Sanders & Fabian 2007; Russell et al. 2008). Assuming spherical symmetry, DSDEPROJ takes the background-subtracted spectra and performs a geometric deprojection starting from the outermost annulus and subtracting the projected emission off each successive annulus (Fabian et al. 1981; Kriss et al. 1983). The routine was modified to include a correction for the regions excluded due to point sources and a correction for the difference in effective area between obs. ID 352 and the summed spectra.

The resulting deprojected spectra were each fitted in XSPEC with absorbed single and two-temperature APEC models (Balucinska-Church & McCammon 1992; Smith et al. 2001). The cluster redshift was fixed to $z = 0.0044$ and the absorption of the cluster gas component was fixed to the Galactic column density (Kalberla et al. 2005), consistent with previous analyses (eg. Forman et al. 2007; Million et al. 2010; Werner et al. 2010). The temperature, metallicity and normalization parameters were left free and the χ^2-statistic was minimised for the spectral fit. For the two-temperature spectral fits, the metallicity was tied between the two components. An additional absorbed power-law component was included to account for the nuclear PSF contribution in the spectral fit to the summed spectra. If the power-law parameters are left free, the contribution of the nuclear PSF is incorrectly interpreted in the spectral fitting as hot cluster emission. The parameters of the power-law component were therefore fixed to the best-fit values determined from spectral fitting to deprojected ChaRT/MARX simulated spectra (eg. Russell et al. 2010; Siemiginowska et al. 2010). We also generated a deprojected electron density profile with finer radial binning from the PSF and background subtracted surface brightness profile incorporating the temperature and metallicity variations (eg. Cavagnolo et al. 2009). Finally, the use of the summed spectra was verified by comparing the spectral fit to the summed projected spectra with a simultaneous fit to all of the individual projected spectra in XSPEC. The best-fit parameters for each case were found to agree to within the errors.

3 RESULTS

Using a ChaRT/MARX simulation to subtract the nuclear PSF emission, we are able to determine the gas density down to 1 arcsec radius from the nucleus and the temperature down to 2 arcsec radius. Fig. 3 shows the deprojected single temperature best-fit results using radial bins of $2 - 4$ arcsec width within the central 14 arcsec (1 kpc) region. The deprojected temperature drops from $1.88^{+0.06}_{-0.07}$ keV at 5 kpc (64 arcsec) to $0.91^{+0.08}_{-0.11}$ keV at 0.2 kpc (2.5 arcsec). The coolest X-ray gas is concentrated in the cluster centre (eg. Werner et al. 2010) producing a particularly steep drop in temperature at 1.6 kpc (20 arcsec). The bright, cool rim of the SE cavity is located at a radius of 1 kpc and coincides with an increase in the gas density by a factor of 2. The density drops at a radius of ~ 0.5 kpc due to the SE cavity and this produces larger errors on the deprojected profiles due to the reduced number of counts in this region. The apparent increase in the deprojected tempera-
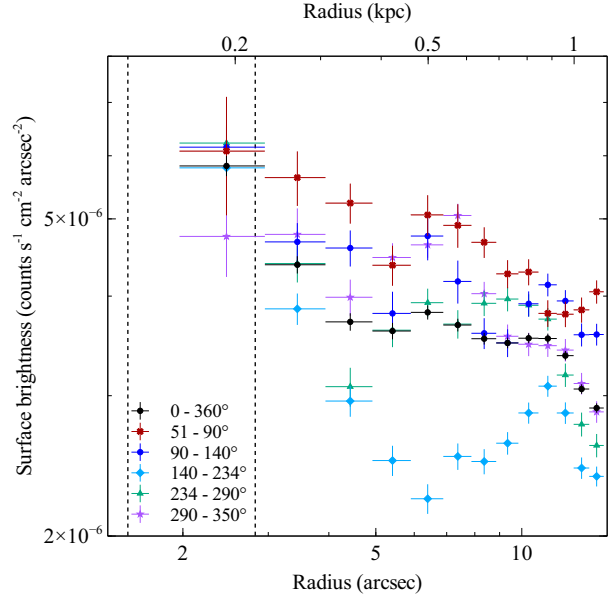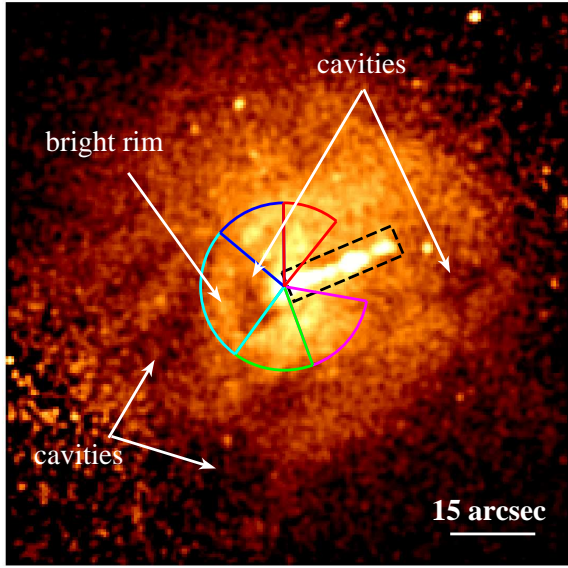
Figure 2. Left: Exposure-corrected image showing the sectors used to compare the angular variation in the cluster surface brightness around the nucleus. The excluded jet region is shown by the dashed black box. Right: Background-subtracted surface brightness profiles in the energy band $0.5 - 7.0$ keV extracted from these sectors. There is a cavity in the sector from $140 - 234°$ which complicates the deprojection analysis. The radial range for the Bondi radius is shown by the vertical dashed lines.

ture at $0.3 - 0.8$ kpc radius is therefore not significant and the profile is consistent with a modest decline in temperature towards the cluster centre. However, it is also clear that a single temperature fit is not adequate and multi-temperature gas is present requiring a two-temperature spectral model. The metal abundance peaks at $1.1 \pm 0.1 \, Z_\odot$ at a radius of 4 kpc and then appears to drop rapidly in the cluster centre. This drop can be caused by the Fe bias that occurs when a single temperature model is fitted to a multi-temperature medium (eg. Buote 2000).
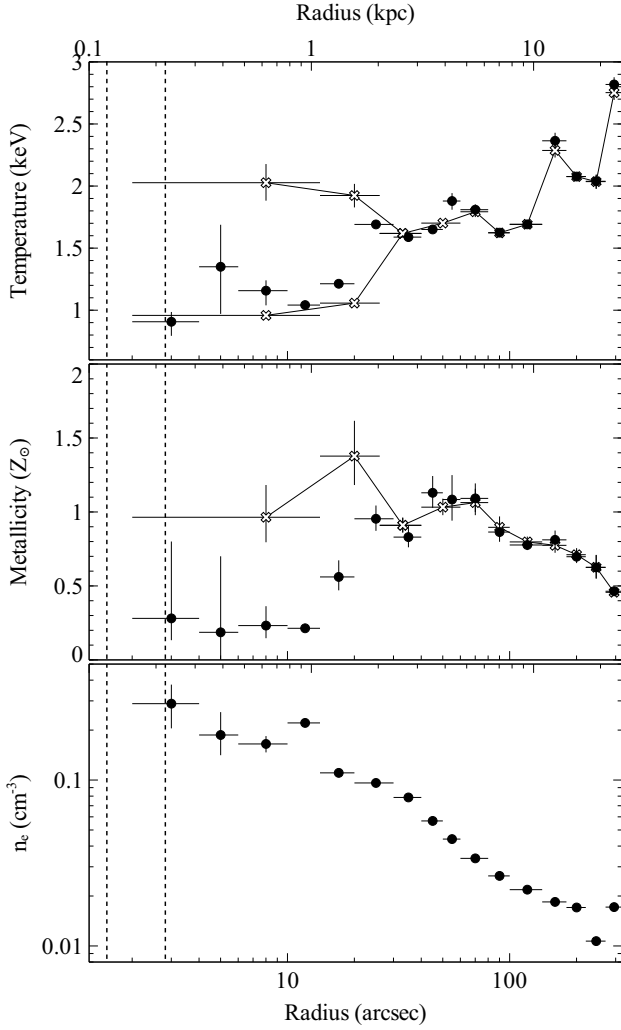
3.1 Two temperature models

Fig. 3 shows the deprojected temperature and metallicity profiles produced by fitting two-temperature models to the spectra extracted in broader radial bins. Within 2 kpc, a second temperature component provides a better representation of the data with an F-test probability $< 0.01\%$ that the second component is detected by chance. The best-fit temperature values are 1.98 ± 0.09 keV and 1.00 ± 0.02 keV. The metallicity now appears to be consistent with $1 \, Z_\odot$ in the cluster centre. By fixing the metallicity to $1 \, Z_\odot$, a two-temperature model was also fitted to the spectra extracted from the cluster centre, within 2 kpc, in narrower radial bins. Fig. 4 shows the resulting deprojected profiles where multi-temperature gas was detected significantly within 2 kpc. In addition to the metallicity constraint, the temperature parameters were fixed to 0.9 keV and 2 keV in the $0.3 - 0.45$ kpc radial bin where the cavity increased the uncertainties. Only the APEC normalization parameters were left free for this region. The gas temperatures for the two components appear roughly constant within 1 kpc, although there could be a modest decrease in the lower temperature component. No evidence was found for a temperature increase at small radii due to the gravitational influence of the black hole, although this may occur at smaller radii within 0.15 kpc.

The temperature profile down to a radius of 2 arcsec was not

significantly affected by the estimated uncertainty in the PSF subtraction. In section 2, the PSF-subtracted cluster surface brightness profiles from obs. ID 1808 and the summed obs. IDs 11513 to 14974 were compared and found to agree within the errors. However, the cluster surface brightness in the $1 - 2$ arcsec radial bin is also consistent with a $\sim 15\%$ difference between the two epochs, which may be due to minor inaccuracies in the PSF subtraction such as an underestimation of the pileup fraction. The nuclear PSF flux is significantly lower in obs. ID 1808 therefore it is more likely that the PSF contribution has been underestimated in the summed observations. To be conservative, we have therefore estimated the impact on the measured gas properties if the PSF flux is higher by 20%. This will increase the oversubtraction within 1 arcsec where the flux has been reduced by pileup but could improve the subtraction of the PSF wings. No significant change in the temperature profile was found for this increase in the PSF flux. We also note that no significant variation in the temperature was found if the PSF flux was instead reduced by 20%. Within 2 arcsec, the nuclear PSF dominates over the cluster emission and the uncertainty in the faint hard X-ray emission above 3 keV produced a large uncertainty in the gas temperature. The gas temperature profile is therefore restricted to radii greater than 2 arcsec.
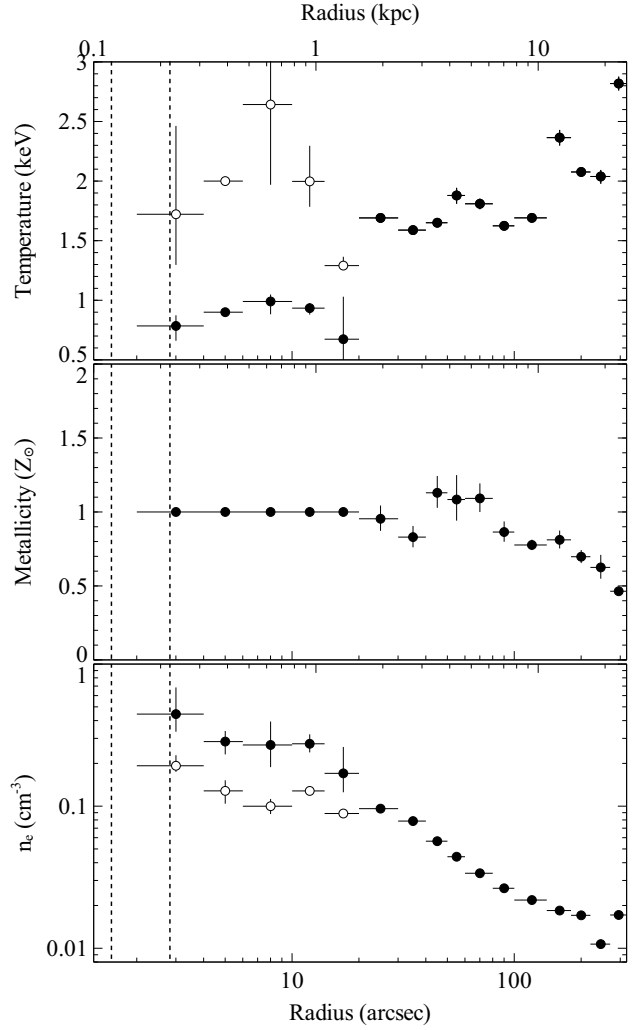
3.2 Density profile

The coolest component of the multi-temperature gas in M87 likely consists of small blobs and filaments whilst the 2 keV component fills the volume, excluding the cavities (Young et al. 2002; Sparks et al. 2004; Werner et al. 2010). By assuming that the different gas phases are in pressure equilibrium, the filling factor of the cooler gas component can be calculated and used to determine the gas density. Note that we have ignored magnetic pressure, which is likely required to support extended filaments of cold gas (Fabian et al. 2008). The gas density of both temperature components continues

Figure 3. Deprojected temperature, metallicity and density profiles comparing a single temperature spectral model (solid circles) and a two temperature spectral model (open crosses). The radial range for the Bondi radius is shown by the vertical dashed lines.


Figure 4. Deprojected temperature, metallicity and density profiles for a two temperature spectral model. The finer radial binning was achieved by fixing the metallicity inside a radius of 1.5 kpc. The density was calculated by assuming pressure equilibrium between the two temperature components. The radial range for the Bondi radius is shown by the vertical dashed lines.

to rise towards the cluster centre and the profile appears to steepen inside 0.5 kpc radius. A similar increase is seen in Fig. 3 for the single temperature density profile. To determine if this steepening is significant, we have also produced a deprojected density profile with narrower 1 arcsec radial bins from the PSF and background-subtracted surface brightness profile (see section 2.2).

Fig. 5 shows the higher spatial resolution density profile which extends in to 1 arcsec. The density profile steepens within 0.3 kpc and peaks at a density of $0.62 \pm 0.05 \, \mathrm{cm}^{-3}$. Measurement of the gradient is however complicated by the cavity at ~ 0.5 kpc radius, where the emitting volume is overestimated and therefore the density is underestimated. Due to the cavity, the majority of the emission at this radius is projected. Therefore the density value is also sensitive to the PSF subtraction despite this accounting for only $\sim 2\%$ of the total emission. The nuclear PSF accounts for roughly half of the total emission in the $1 - 2$ arcsec radial bin and therefore any inaccuracy in the subtraction could have a significant effect here (Fig. 1). Fig. 5 also shows the resulting density profile if the nuclear PSF flux is increased by 20%. The peak density drops to $0.49 \pm 0.06 \, \mathrm{cm}^{-3}$ and the gradient of the profile inside 0.3 kpc ra-

dius is shallower. Fig. 5 shows two possible lines of best-fit to the density profile at the centre of M87. The best-fit power-law slope of -1.2 ± 0.2 assumed that the PSF subtraction is sufficiently accurate and excluded all points beyond a radius of 0.3 kpc. The shallower best-fit slope of -1.0 ± 0.2 was determined using the increased PSF subtraction. The density profile is therefore consistent with $\rho \propto r^{-1}$ within the Bondi radius.

3.3 Cooling time and dynamical time profiles

Multi-temperature structure is expected to form in the ICM when the radiative cooling time of the gas becomes short with respect to the gas dynamical time. Within 2 kpc, a second temperature component is significantly detected in the hot gas and this is also coincident with the extent of the brightest Hα filaments (Young et al. 2002; Sparks et al. 2004). We have therefore calculated the radiative cooling time and dynamical time profiles to determine if this observed structure is consistent with the develop-
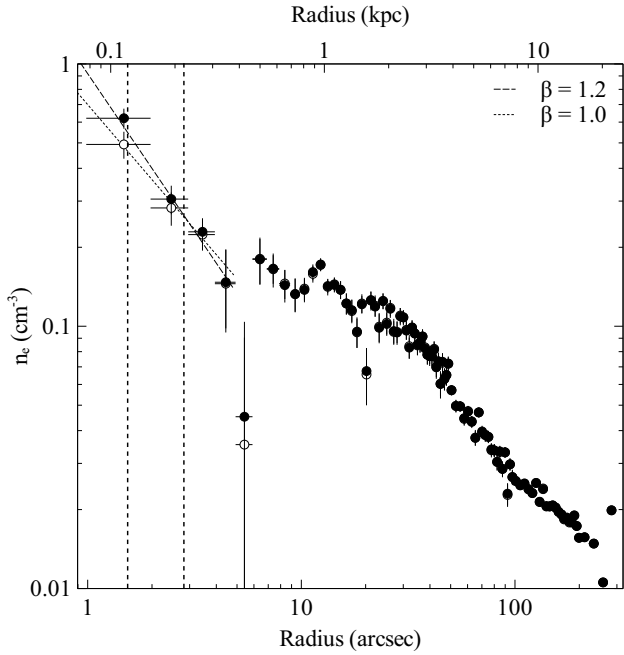
Figure 5. Deprojected density profile. The nuclear flux contribution has been subtracted off using a ChaRT simulation (solid circles). The open circles show the deprojected density profile if the nuclear flux was increased by 20%. The radial range for the Bondi radius is shown by the vertical dashed lines.

Figure 6. Upper panel: the radiative cooling time profile for a single temperature component model and the dynamical free-fall time profile. Lower panel: the ratio of cooling time to free-fall time.

ment of local thermal instabilities. The radiative cooling time, $t_{\rm cool} = (3/2)\,nkT/n^2\Lambda$, was determined from the single component temperature and density profiles. For the two component spectral model, the cooling time is approximately a factor of two longer for the hotter component and a factor of $2-3$ shorter for the colder component. The dynamical time was calculated using the mass profile for M87 of Romanowsky & Kochanek (2001) (see also Chura-zov et al. 2008). Fig. 6 shows the cooling time, the free-fall time and the $t_{\rm cool}/t_{\rm ff}$ profiles for M87. The radiative cooling time drops to $3\pm2\times10^7$ yr at 0.2 kpc and is even shorter for the cool X-ray temperature component at $(1.1\pm0.8)\times10^7$ yr. The ratio reaches a minimum of $t_{\rm cool}/t_{\rm ff} = 16\pm2$ at a radius of 0.9 kpc and is comparably low to a radius of ~ 4 kpc.
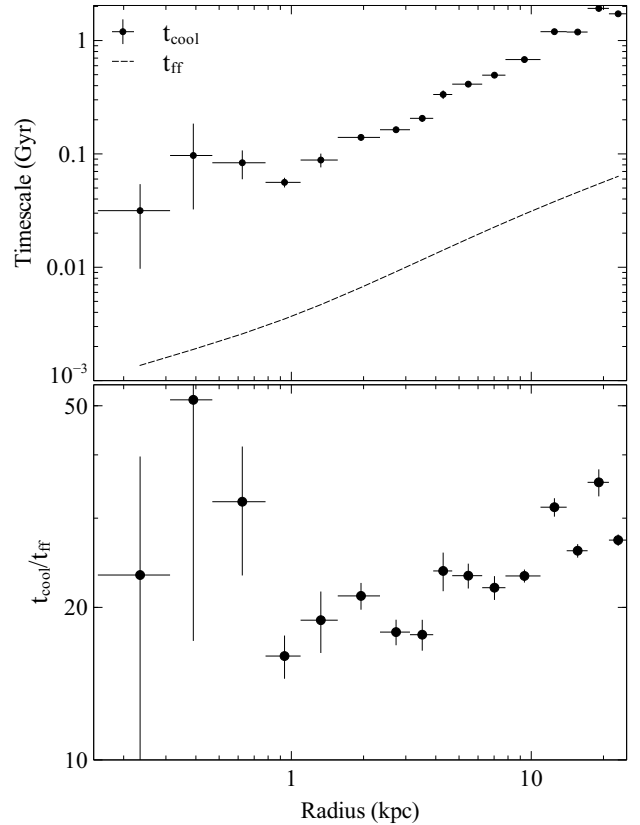
3.4 Bondi radius and accretion rate

The SMBH should accrete from the surrounding hot atmosphere at a rate determined by its mass and the gas density and temperature at the radius where the SMBH's gravitational influence dominates (Bondi 1952). Under the assumptions of spherical symmetry and negligible angular momentum, the Bondi accretion rate is given by

$$\frac{\dot{M}_{\rm B}}{{\rm M}_\odot\,{\rm yr}^{-1}} = 0.012\left(\frac{k_{\rm B}T}{\rm keV}\right)^{-3/2}\left(\frac{n_e}{{\rm cm}^{-3}}\right)\left(\frac{M_{\rm BH}}{10^9\,{\rm M}_\odot}\right)^2, \quad (1)$$

where T the gas temperature, n_e is the gas electron density and $M_{\rm BH}$ is the SMBH mass. An adiabatic index $\gamma = 5/3$ is assumed. The Bondi radius can also be expressed as

$$\frac{r_{\rm B}}{\rm kpc} = 0.031\left(\frac{k_{\rm B}T}{\rm keV}\right)^{-1}\left(\frac{M_{\rm BH}}{10^9\,{\rm M}_\odot}\right). \quad (2)$$

Recent gas-dynamical and stellar-dynamical black hole mass estimates for M87 differ by a factor of two from $M_{\rm BH} = 6.6\pm0.4\times10^9\,{\rm M}_\odot$ (Gebhardt et al. 2011) to $M_{\rm BH} = 3.5^{+0.9}_{-0.7}\times10^9\,{\rm M}_\odot$ (Walsh et al. 2013). Therefore, our estimates of the Bondi radius and accretion rate are expressed as a range covering these two values of the black hole mass.

For a single temperature spectral model, the temperature falls to $0.91^{+0.08}_{-0.11}$ keV in the centre of M87 and therefore the Bondi radius $r_{\rm B} = 0.12 - 0.22$ kpc ($1.5 - 2.8$ arcsec). The electron density at the Bondi radius ranges between $0.31\pm0.04\,{\rm cm}^{-3}$ and $0.62\pm0.05\,{\rm cm}^{-3}$, which gives Bondi accretion rates $\dot{M}_{\rm B} = 0.1 - 0.2\,{\rm M}_\odot\,{\rm yr}^{-1}$. Assuming a standard $\sim 10\%$ efficiency and accretion onto the SMBH at the Bondi rate, the Bondi accretion power is $P_{\rm B} = 0.5 - 1\times10^{45}$ erg s^{-1}. Bondi accretion therefore would be sufficient to fuel the mechanical power output from the jet of $P_{\rm jet} = 8^{+7}_{-3}\times10^{42}$ erg s^{-1} (eg. Bicknell & Begelman 1999; Di Matteo et al. 2003; Rafferty et al. 2006; Russell et al. 2013). If we consider only the higher, volume-filling temperature component of the two temperature spectral model, the Bondi accretion rate would be a factor of ~ 5 lower but still sufficient to power the jet. For a nuclear bolometric luminosity $L_{\rm bol} \sim 2\times10^{41}$ erg s^{-1}, the Bondi accretion power is also far greater than the nuclear radiation losses (Reynolds et al. 1996; Di Matteo et al. 2003). Both the accretion flow and the jets are therefore radiatively inefficient (Di Matteo et al. 2003), although the accretion rate may be much lower at the event horizon.

4 DISCUSSION

The gas density and temperature profiles within the accretion radius may in principle reflect the gravitational influence of the central SMBH and permit us to distinguish between different accretion flow models. M87 is one of only a few systems with a Bondi radius that can be resolved by *Chandra* but the analysis is complicated by the bright central point source and jet emission. By stacking short frame-time observations of M87 taken after the HST-1 flaring period and using a ChaRT/MARX simulation to subtract the PSF, we determined the gas density to within the Bondi radius and traced the multi-temperature structure on these spatial scales.

4.1 Hot gas accretion

Within 2 kpc, two temperature components are significantly detected, which are consistent with constant values of 2 keV and 0.9 keV down to a radius of 0.15 kpc. No evidence was found for an increase in gas temperature within ~ 0.25 kpc radius where the SMBH is expected to gravitationally heat the ambient gas, although this may occur at small radii within 0.15 kpc (eg. Brighenti & Mathews 1999; Quataert & Narayan 2000). Evidence for central temperature increases on this scale has been found in several nearby elliptical galaxies (Pellegrini et al. 2003; Machacek et al. 2006; Humphrey et al. 2008; Pellegrini et al. 2012) and, in NGC3115, the hotter, volume-filling component of a two temperature model appears to increase to ~ 1 keV towards the centre (Wong et al. 2014).

However, the hot atmosphere at the centre of M87 has been significantly disturbed by the AGN. Several X-ray cavities are co-incident with radio jet emission in the core of M87, including one at a radius of only 0.5 kpc to the SE of the nucleus in the counter-jet direction (Young et al. 2002; Forman et al. 2005, 2007). This activity will generate shocks, stir up the gas and cause departures from hydrostatic equilibrium (eg. Forman et al. 2005; Churazov et al. 2008). The counter-jet cavity corresponds to a region of apparent low pressure and high projected temperature (Million et al. 2010; Werner et al. 2010). The hotter ~ 2 keV component of the multi-temperature ICM inside a radius of ~ 2 kpc may correspond to gas heated by this recent jet outburst. The multi-temperature structure could therefore be due to hotter, shock-heated regions and dense clumps of cooling gas but this cannot be distinguished from a more homogeneous multi-temperature distribution by the azimuthally-averaged temperature profiles. Finer spatial binning of the temperature profile extending in to 1 arcsec radius, excluding the region affected by the AGN activity and tracing any azimuthal variation may be possible with additional observations if the nuclear flux continues to decline. However, with the existing data, the central temperature gradient is likely affected by the AGN activity and may not reflect the underlying gravitational potential.

The density profile was extracted using finer spatial bins, which extend in to 1 arcsec, and is also more robust to uncertainties in the PSF subtraction. The profile flattens within ~ 3 kpc with a ridge of increased density at 1 kpc (~ 12.5 arcsec) corresponding to the bright rim of the inner bubble. From the density and temperature profiles, we calculated the Bondi accretion rate $\dot{M}_B = 0.1 - 0.2 M_\odot$ yr^{-1} across the Bondi radius located at $0.12 - 0.22$ kpc ($1.5 - 2.8$ arcsec), depending on the black hole mass. For accretion onto the SMBH at the Bondi rate and assuming 10% efficiency, the accretion rate is roughly two orders of magnitude greater than that required by the mechanical power output of the jet. The density profile for a Bondi flow is given by $\rho \propto r^{-\beta}$, where $\beta = 3/2$ for $r \ll r_B$. Close to the Bondi radius, on the scales probed by the *Chandra* observations, a Bondi flow has a shallower gradient, $\beta < 1$ (Bondi 1952; Narayan & Yi 1994; Quataert & Narayan 2000). Excluding the region affected by the cavity, the density profile inside the Bondi radius in M87 is consistent with $\rho \propto r^{-1}$, which may indicate the onset of a Bondi flow. However, the ADIOS and CDAF models are also supported by a shallow density profile and cannot be ruled out by the existing observations. Alternatively, the density profile could reflect the radio jet activity rather than the underlying gravitational potential. *Chandra* observations of NGC 4889, one of two BCGs in the Coma cluster with a black hole mass of $2 \times 10^{10} M_\odot$ (McConnell et al. 2011), show a central cavity inside 0.6 kpc radius, which is comparable to the recent outburst in M87 (Sanders et al. 2014). The density distribution is consistent with no X-ray emission within this radius suggesting that much of the material has been driven out by the jet. Although we cannot rule out the different models, it is not clear that the hot gas structure across the Bondi radius is dictated by the gravitational potential of the SMBH and the classical Bondi accretion rate may not reflect the accretion rate onto the SMBH.

4.2 Hot outflow?

Faraday rotation measurements can provide constraints on the accretion rate much closer to the SMBH on scales of tens of Schwarzschild radii (r_s). For M87, Kuo et al. (2014) determined an upper limit on the accretion rate at $21 r_s$ of $9.2 \times 10^{-4} M_\odot$ yr^{-1}. This limit is at least two orders of magnitude below the Bondi rate and it is consistent with the density profile $\rho \propto r^{-1}$, determined by *Chandra*, extending in to this radius. However, this analysis assumes that the observed Faraday rotation originates in the accretion flow, the density profile follows a power-law with $\beta \leq 3/2$ and an equipartition strength magnetic field.

Observations of Sgr A* and NGC3115 are consistent with the onset of an accretion flow inside the Bondi radius and a reduced accretion rate onto the SMBH. Using a 1 Ms *Chandra* observation of NGC3115, Wong et al. (2014) found a shallow density profile, $\rho \propto r^{-1}$, and a hot gas component with increasing temperature within the Bondi radius reflecting the gravitational potential of the SMBH. For Sgr A*, Wang et al. (2013) showed that the density profile is consistent with $\rho \propto r^{-1/2}$, assuming a temperature profile $T \propto r^{-1}$. Faraday rotation measurements of Sgr A* provide an upper limit on the accretion rate at $r \leq 100 r_s$ (Bower et al. 2003; Marrone et al. 2006, 2007; Macquart et al. 2006). When combined with the X-ray measurements at the Bondi radius, this suggests that the flat density profile covers a broad radial range down to $r \sim 100 r_s$ indicating little material captured at the Bondi radius reaches the SMBH (Yuan et al. 2003; Wang et al. 2013).

These observations are consistent with numerical simulations and analytical models of hot accretion flows, with accretion rate decreasing with decreasing radius so that the majority of the material is lost between the Bondi radius and the event horizon (eg. Igumenshchev & Abramowicz 1999; Stone et al. 1999; Stone & Pringle 2001; Hawley & Balbus 2002; Yuan & Bu 2010; Begelman 2012). The radial density profile becomes correspondingly flatter with $\rho \propto^{-(0.5-1)}$. Recent simulations by Yuan et al. (2012) covering a greatly expanded radial range found density profiles described by $\rho \propto^{-(0.65-0.85)}$ for $r > 10 r_s$, favouring the ADIOS model where the majority of the mass is blown out in a wind (Yuan et al. 2012).

If the accretion rate onto the SMBH in M87 is similarly reduced from the Bondi rate to $\dot{M}_{BH} = 9.2 \times 10^{-4} M_\odot$ yr^{-1} (at $21 r_s$, Kuo et al. 2014), the accretion power is $P_{BH} = 5 \times 10^{42}$ erg s^{-1}, where an efficiency of 10% has been assumed. This is two or-

ders of magnitude below the Bondi accretion power and close to the mechanical power output generated by the jet $P_{\rm jet} = 8^{+7}_{-3} \times 10^{42}$ erg s^{-1}. The bulk of the mass flow will presumably be lost in a wind, which will deposit mass and momentum in the surrounding ambient gas (eg. Proga & Begelman 2003; Ostriker et al. 2010). This will reduce the inflow, controlling the growth of the SMBH and making the accretion flow time variable. Calculation of the Bondi rate also assumes that the hot gas at the Bondi radius is falling toward the SMBH. Instead, the temperature profile indicates the hot gas dynamics may not be dictated by the SMBH and the metallicity structure and ionized gas dynamics suggest outflow. The alignment of cool, metal-rich gas with the radio jet and cavity axes is consistent with a jet-driven outflow of gas uplifted from the cluster centre (Belsole et al. 2001; Matsushita et al. 2002; Molendi 2002; Simionescu et al. 2008; Kirkpatrick et al. 2011). The most recent AGN outburst generated the inner radio bubbles $\sim 10^7$ yr ago and uplifted roughly $5 \times 10^8 \, {\rm M_\odot}$ of gas to ~ 20 kpc radius (Simionescu et al. 2008).

The state of the hot gas in M87 differs from the cold gas disk, which is clearly dictated by the SMBH (Harms et al. 1994; Macchetto et al. 1997; Walsh et al. 2013). The central ionized gas disk rotates at velocities from -500 to $+500$ km s^{-1} with a mass of $\sim 4 \pm 1 \times 10^3 \, {\rm M_\odot}$ inside 1 arcsec radius (Ford et al. 1994; Harms et al. 1994; Macchetto et al. 1997). However, optical and UV observations of extended dusty gas filaments found broad emission lines with both blue and redshifted non-Keplerian components at several hundred km/s with respect to the systemic velocity (Tsvetanov et al. 1998; Ford & Tsvetanov 1999). Several filaments appear to connect to the disk and the kinematics of the inner filaments are consistent with a bi-directional wind blowing from the disk (Sparks et al. 1993; Ford & Tsvetanov 1999). The preponderance of evidence supports an outflow from the hot gas and the disk of cold gas.

4.3 Cold inflow?

Most of the circumnuclear gas in the rotating disk is presumably in the form of molecular clouds but currently only tentative detections and upper limits typically of several $\times 10^6 \, {\rm M_\odot}$ have been found (Braine & Wiklind 1993; Combes et al. 2007; Tan et al. 2008; Salomé & Combes 2008). Loss of angular momentum through collisions between clouds and the wind blowing off the disk could allow this gas to flow inwards and fuel the SMBH. In the 'cold feedback' model, these circumnuclear gas disks can be fed by overdense, thermally unstable blobs of gas that cool rapidly from the surrounding hot atmosphere and lose angular momentum through drag in the ICM to accrete onto the disk (Pizzolato & Soker 2005; Nulsen 1986; Pizzolato & Soker 2010). Short central radiative cooling times in the hot ICM are strongly correlated with the presence of extended cool gas filaments suggesting that these originate in cooling of the hot gas (Heckman 1981; Cowie et al. 1983; Peres et al. 1998).

Fig. 3 shows that the hot gas in M87 is multi-temperature within 2 kpc, which coincides with the extent of the brightest Hα filaments (Young et al. 2002; Sparks et al. 2004; Werner et al. 2010). Numerical simulations of thermal instability in the ICM suggest that this multi-temperature structure will form when the gas cooling time drops to a factor of ten greater than the dynamical free-fall time, $t_{\rm cool}/t_{\rm ff} \lesssim 10$ (McCourt et al. 2012; Sharma et al. 2012; Voit et al. 2014). The ratio of the radiative cooling time to the free-fall time in M87 drops to $t_{\rm cool}/t_{\rm ff} = 16 \pm 2$ at 0.9 kpc and

is comparably low to a radius of ~ 4 kpc. This appears inconsistent with the criterion for multi-temperature gas where $t_{\rm cool}/t_{\rm ff} \lesssim 10$ but Voit et al. (2014) suggest that AGN feedback can cause the minimum ratio value to fluctuate and a broader range of values may be acceptable. Pizzolato & Soker (2005) show that, in addition to short cooling times and a suppressed rate of thermal conduction, the ambient density profile must be shallow for cold feedback to occur. Overdense, rapidly cooling gas will be prevented from reaching an equilibrium position in the ICM and can cool to low temperatures. The most significant flattening of the density profile in M87 occurs at ~ 3 kpc radius, which also encompasses the brightest Hα emission and multi-temperature ICM structure.

The radiative cooling time drops to only 10^7 yr for the cooler X-ray temperature component inside 4 arcsec radius. There are clear associations between the soft X-ray emission and the optical line filaments (Sparks et al. 2004) and, whilst the innermost filaments are outflowing, the outer filaments appear to be falling in towards the disk (Sparks et al. 2004). These overdense, rapidly cooling gas clouds can decouple from the ICM and nearly free-fall to the cluster centre (Pizzolato & Soker 2010). At 0.2 kpc radius, the cool X-ray gas component represents $\sim 20\%$ of the total X-ray gas mass and could lose angular momentum to the hot gas component if this is not rotating. The cooler X-ray temperature component could therefore provide a source of cold gas clouds within the Bondi radius with a mass deposition rate of $\sim 0.1 \, {\rm M_\odot}$ yr^{-1}. This would produce sufficient fuel to power the most recent radio jet outburst. The X-ray mass deposition rate measured by the *XMM-Newton* RGS in a 1.1 arcmin wide aperture (5.2 kpc) is $\dot{M} = 0.9 \, {\rm M_\odot}$ yr^{-1} for gas cooling radiatively from 1 keV to 0.5 keV and $\dot{M} < 0.06 \, {\rm M_\odot}$ yr^{-1} below 0.5 keV (Werner et al. 2010). However, if the coolest X-ray gas mixes with the cold Hα-emitting filaments, which may be promoted by the AGN activity, then there could be significant non-radiative cooling of the gas (Fabian et al. 2002; Soker et al. 2004; Sanders et al. 2010). Taken together, the data are consistent with cold feedback where gas cooling from the hot ICM feeds the circumnuclear gas disk.

5 CONCLUSIONS

Using recent short frame-time *Chandra* observations of M87 taken after the flaring period of the HST-1 jet knot, we have subtracted the nuclear PSF to determine the temperature and density structure of the hot gas within the Bondi accretion radius. Within 2 kpc, we detect two significant temperature components, which are consistent with constant values of 2 keV and 0.9 keV down to a radius of 0.15 kpc. No evidence was found for the expected increase in the gas temperature within a radius of ~ 0.25 kpc, where the SMBH is expected to gravitationally heat the surrounding gas. This may occur at smaller radii within 0.15 kpc.

From the temperature and density profiles, we calculated the Bondi accretion rate of $0.1 - 0.2 \, {\rm M_\odot}$ yr^{-1} across the Bondi radius at $0.12 - 0.22$ kpc ($1.5 - 2.8$ arcsec), depending on the black hole mass. The density profile flattens inside 3 kpc and then steepens again within 0.3 kpc (4 arcsec) to peak at $0.5 - 0.6$ cm^{-3}. Inside the Bondi radius, the density profile is consistent with $\rho \propto r^{-1}$. Whilst a temperature rise within 0.15 kpc cannot be ruled out, the absence of the expected temperature increase inside the Bondi radius indicates that the hot gas dynamics are not dictated by the SMBH and, together with the shallow density gradient, suggests that the classical Bondi rate may not reflect the SMBH's accretion rate. If this shallow density gradient extends inwards to the SMBH, consistent with

the Faraday rotation measurements for M87, the accretion rate onto the SMBH could be two orders of magnitude below the Bondi rate. Whilst this is still sufficient to power the recent radio jet outburst, assuming an efficiency of 10%, the accretion flow will be significantly altered if a wind blows out the majority of the mass. The uplift of metal-rich gas along the radio jet axis and broad optical and UV emission lines in the ionized gas disk support the existence of an outflow in the hot gas and the cold gas disk.

Clear associations exist between the coolest X-ray gas and the optical line-emitting filaments at the centre of M87 and several outer filaments appear to be infalling towards the disk. Observations show that the ICM has multiple temperature components inside a radius of 2 kpc, the radiative cooling time of the coolest X-ray gas drops to 10^7 yr here and this rapidly cooling gas is co-incident with the extent of the bright Hα emission. The density profile also flattens significantly at this radius, which is consistent with cold feedback models that suggest a shallow density profile will prevent overdense, cooling blobs from reaching an equilibrium position. The cooler X-ray temperature component could provide a source of cold gas clouds within the Bondi radius and sufficient fuel to power the most recent radio jet outburst.

APPENDIX: SIMULATING THE NUCLEAR PSF

A1 Pileup

Two or more photons landing on the same ACIS detector region within the same frame integration time will be detected as a single event. Known as pileup (see eg. Davis 2001), the photon energies sum to make a detected event of higher energy. The source spectrum hardens and the altered shape of the charge cloud distribution can cause grade migration, where the event is misidentified as a cosmic ray and excluded from analysis. Most of the intensity of piled up sources should still be recovered. However, when the jet knot HST-1 was near its peak, strong pileup produced events that exceeded the energy filter cutoff and were not telemetered to the ground resulting in lost flux (Harris et al. 2009). The proximity of HST-1 to the bright nucleus also produced the 'eat-thy-neighbour' effect where photons arriving within the same frame and 3×3 pixel grid are considered part of the same event. The photon with the most energy then determines the recorded location for both (Harris et al. 2009). It was therefore important to determine the extent of any pileup in the observations used and whether it was possible to accurately subtract the nuclear PSF from the surrounding extended emission.

The pileup fraction was estimated using the ratio of 'good' event grades to 'bad' grades in a region of 1 arcsec radius centred on the emission peak. Most of the nuclear emission comes from the $0.5 - 2$ keV energy band which, if piled up, increases the number of higher energy events above 2 keV with 'bad' grades. We therefore used the ratio of 'bad' to 'good' grades in the $2 - 5$ keV energy band as an estimate of the pileup fraction but note that this measure is dependent on the nuclear spectrum and affected by onboard rejection. This analysis was confirmed in section A3 with a MARX simulation of the nuclear PSF that included a statistical treatment of pileup (Davis 2001).

Apart from obs. ID 352, all of the observations used have a short frame integration time of 0.4 s to reduce pileup. We estimate that obs. ID 1808 has the lowest pileup fraction at 6% and the more recent observations taken since 2010 have a slightly higher pileup fraction of $10 - 15\%$ because the nucleus was a factor of $\sim 1.5 - 2$ brighter. Obs. ID 352 has a standard frame integration time of 3.2 s and is therefore strongly piled up by $\sim 80\%$. Following Harris et al. (2006), the brightness of HST-1 was determined using a detector-based measure of intensity (keV s^{-1}), which sums the photon energies from the event 1 file with no grade filtering. The HST-1 brightness drops from 0.3 keV s^{-1} in 2010 to 0.2 keV s^{-1} at the end of 2012. These measurements are all more than an order of magnitude below the 4 keV s^{-1} limit above which Harris et al. (2009) suggest that more complex pileup problems occur. The measurements also confirm that HST-1 has returned to the 2000 brightness level before the major flare and pileup is now only mild for observations with a frame integration time of 0.4 s.

A2 Nuclear spectrum

For each observation, we extracted a nuclear spectrum using a region of 1 arcsec radius centred on the nuclear emission peak. We assume that all emission within 1 arcsec is from the AGN. However the gas emission is likely to be $\sim 5\%$ of the total, depending on the slope of the gas density profile. A corresponding background spectrum, including the cluster emission, was extracted using a surrounding annulus from $2 - 4$ arcsec. The spectra were restricted to the $0.5 - 7$ keV energy band and appropriate responses and ancillary responses were generated. The spectra were fitted individually in XSPEC version 12.8.2 (Arnaud 1996) with an absorbed power law model. All parameters were left free and the modified version of the C-statistic available in XSPEC was used to determine the best-fit values (Cash 1979; Wachter et al. 1979). Comparing the observation in 2000 with those in 2010 to 2013, there has been modest variation in the best-fit photon index and the absorption parameter, $n_{\rm H}$ (Table 1), which was consistently above the Galactic value of 0.019×10^{22} cm^{-2} (Kalberla et al. 2005). The nuclear flux varies by up to a factor of a few, which is consistent with previous studies (eg. Harris et al. 1997, 2009). The spectra for obs. IDs 11513 to 14974 were also fitted simultaneously in XSPEC to determine the average best-fit model, weighted by the exposure, for the ChaRT simulation. The best-fit parameters for this 'stacked' spectrum are given in Table 1.

A3 ChaRT simulations

From the nuclear spectral model and the source position in mirror spherical coordinates, the ChaRT program (Carter et al. 2003)
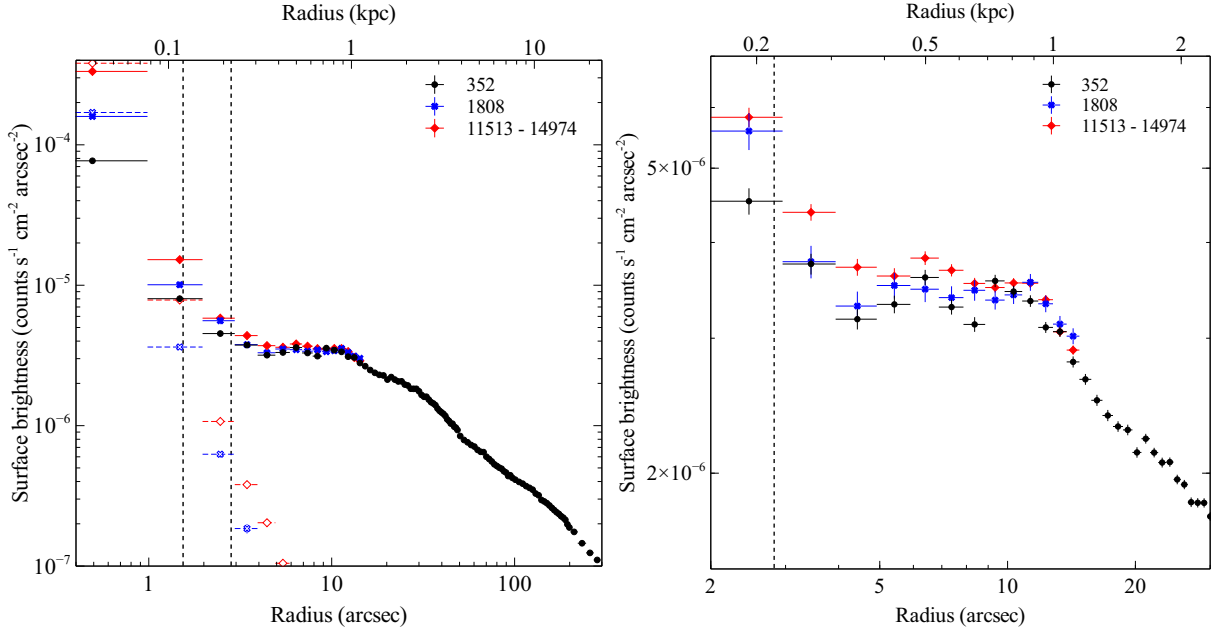
Figure 7. Left: Background-subtracted surface brightness profiles in the energy band $0.5 - 7.0$ keV for obs. ID 352, obs. ID 1808 and summed obs. IDs 11513 to 14974. The open symbols show the predicted contribution to the total emission by the nuclear PSF from the ChaRT simulations for obs. IDs 11513 to 14974 (red) and obs. ID 1808 (blue). The radial range for the Bondi radius is shown by the vertical dashed lines. Right: Zoom in showing the region of overlap between the subarray and full frame datasets.

and the MARX software[1] were used to simulate the nuclear PSF. ChaRT provides an interface to the SAOTrace raytrace code, which is based on the most accurate mirror model and incorporates the details of the support structures and baffles (Jerius et al. 1995). ChaRT simulations of the PSF core and inner wings out to 10 arcsec match well with on-axis observations (Jerius 2002). The M87 nucleus was on-axis in each observation analysed and the nuclear emission is only significant compared to the cluster emission to 3 arcsec radius. Therefore the ChaRT simulations should provide a good reconstruction of the PSF. Multiple ray-traces were used and analysed simultaneously to ensure sufficient photons for a detailed comparison with the observations. MARX version 4.5 was used to project the ChaRT raytraces onto the ACIS-S detector and account for the effects of the detector response. Although some differences exist between the MARX ACIS effective area and that observed, the excellent agreement between the subtracted profiles in Fig. 1 shows that this is not a significant effect. MARX also includes the standard effects of the dither motion and residual blur from aspect reconstruction errors using the DitherBlur parameter.

From the simulated events file, an exposure-corrected image in the $0.5 - 7$ keV energy band was generated with spectral weighting determined by the nuclear emission model in section A2. A surface brightness profile for the simulated PSF was extracted from this image using a series of concentric annuli of 1 arcsec width. A surface brightness profile was also generated for each of the M87 observations from an exposure-corrected image weighted by a spectral model for the cluster emission in the core (section 2.2). The surface brightness profiles for the obs. IDs 11513 to 14974 were then stacked to produce an average profile. The short frame integration times of these observations, and obs. ID 1808, required the use of a subarray to reduce the readout time and avoid losing data. The

resulting surface brightness profiles only extended to a radius of 15 arcsec and therefore, despite strong pileup in the centre, obs. ID 352 was used to trace the cluster gas to larger radii.

The surface brightness profiles for the M87 observations and the PSF simulations are shown in Fig. 7. The nuclear emission clearly dominates over the extended cluster emission inside a radius of 2 arcsec. The profiles appear consistent beyond a radius of ~ 5 arcsec as expected if all variable point sources have been excluded from the cluster emission. Although there has been a significant reduction in the effective area at low energies over time due to the build up of contaminant (Marshall et al. 2004), and this has accelerated since 2009, there is still reasonable agreement in the cluster surface brightness for the region of overlap between the datasets (Fig. 7 right). However, within ~ 5 arcsec, variation in the nuclear flux between the observations produces significant differences. The nucleus was brighter for the stacked observations taken from 2010 to 2013 compared to obs. ID 1808, which was taken in 2000. Obs. ID 352 has a 3.2 s frame integration time and is therefore strongly piled up to a radius of 3 arcsec, which reduces the flux detected in the $0.5 - 7$ keV energy band.

The stacked $11513 - 14974$ observations were mildly piled up, which reduced the measured nuclear flux from the central $0 - 1$ arcsec region over that in the PSF wings. The PSF simulation was repeated using MARX to include a statistical realisation of pileup (Davis 2001). This piled up simulation was used to estimate the effect on the nucleus model spectrum and showed that the $0.5 - 7$ keV flux in the central region drops by a factor of ~ 1.15 with little effect in the surrounding annuli. The flux of the PSF simulation was therefore increased to compensate but, while this was a sufficient correction for the normalization, there was also a low level hardening of the spectrum. The soft emission from the hot gas that is also present at the $\sim 5\%$ level within 1 arcsec radius
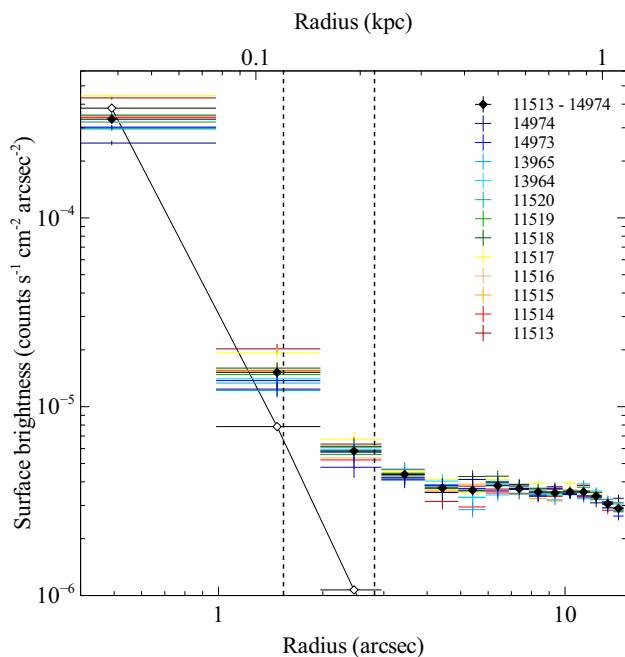
Figure 8. Background-subtracted surface brightness profiles in the energy band $0.5 - 7.0$ keV for the summed and individual obs. IDs used in this analysis. The solid line shows the ChaRT simulation of the nuclear flux. The radial range for the Bondi radius is shown by the vertical dashed lines.

could reduce this effect. However, this uncertainty has limited the temperature measurements at small radii in this analysis.

Fig. 8 shows the surface brightness profiles for each of the observations taken from 2010 to 2013. The nuclear flux varies modestly over this period but beyond 2 arcsec radius the profiles are consistent. We note that the increased uncertainty in the $5 - 6$ arcsec radial bin is due to the presence of a cavity in the X-ray emission and there are fewer counts in this region. Apart from the central source, there do not appear to be any variable point sources that have not been removed from the analysis. The ChaRT/MARX simulations were tested by comparing the PSF-subtracted surface brightness profiles for obs. ID 1808 and the stacked 11513 to 14974 observations as described in section 2.

REFERENCES

Arnaud K. A., 1996, in Astronomical Society of the Pacific Conference Series, Vol. 101, Jacoby G. H., Barnes J., ed, Astronomical Data Analysis Software and Systems V, p. 17

Baganoff F. K. et al., 2003, ApJ, 591, 891

Balucinska-Church M., McCammon D., 1992, ApJ, 400, 699

Begelman M. C., 2012, MNRAS, 420, 2912

Belsole E. et al., 2001, A&A, 365, L188

Bicknell G. V., Begelman M. C., 1996, ApJ, 467, 597

Bicknell G. V., Begelman M. C., 1999, in Lecture Notes in Physics, Berlin Springer Verlag, Vol. 530, Röser H.-J., Meisenheimer K., ed, The Radio Galaxy Messier 87, p. 235

Blandford R. D., Begelman M. C., 1999, MNRAS, 303, L1

Blandford R. D., Begelman M. C., 2004, MNRAS, 349, 68

Bohringer H., Nulsen P. E. J., Braun R., Fabian A. C., 1995, MNRAS, 274, L67

Bondi H., 1952, MNRAS, 112, 195

Bower G. C., Wright M. C. H., Falcke H., Backer D. C., 2003, ApJ, 588, 331

Bower R. G., Benson A. J., Malbon R., Helly J. C., Frenk C. S., Baugh C. M., Cole S., Lacey C. G., 2006, MNRAS, 370, 645

Braine J., Wiklind T., 1993, A&A, 267, L47

Brighenti F., Mathews W. G., 1999, ApJ, 527, L89

Buote D. A., 2000, MNRAS, 311, 176

Carter C., Karovska M., Jerius D., Glotfelty K., Beikman S., 2003, in Astronomical Society of the Pacific Conference Series, Vol. 295, Payne H. E., Jedrzejewski R. I., Hook R. N., ed, Astronomical Data Analysis Software and Systems XII, p. 477

Cash W., 1979, ApJ, 228, 939

Cavagnolo K. W., Donahue M., Voit G. M., Sun M., 2009, ApJS, 182, 12

Churazov E., Forman W., Jones C., Böhringer H., 2000, A&A, 356, 788

Churazov E., Forman W., Vikhlinin A., Tremaine S., Gerhard O., Jones C., 2008, MNRAS, 388, 1062

Combes F., Young L. M., Bureau M., 2007, MNRAS, 377, 1795

Cowie L. L., Hu E. M., Jenkins E. B., York D. G., 1983, ApJ, 272, 29

Croton D. J. et al., 2006, MNRAS, 365, 11

Davis J. E., 2001, ApJ, 562, 575

Di Matteo T., Allen S. W., Fabian A. C., Wilson A. S., Young A. J., 2003, ApJ, 582, 133

Di Matteo T., Quataert E., Allen S. W., Narayan R., Fabian A. C., 2000, MNRAS, 311, 507

Fabian A. C., Allen S. W., Crawford C. S., Johnstone R. M., Morris R. G., Sanders J. S., Schmidt R. W., 2002, MNRAS, 332, L50

Fabian A. C., Canizares C. R., 1988, Nat, 333, 829

Fabian A. C., Hu E. M., Cowie L. L., Grindlay J., 1981, ApJ, 248, 47

Fabian A. C., Johnstone R. M., Sanders J. S., Conselice C. J., Crawford C. S., Gallagher J. S., III, Zweibel E., 2008, Nat, 454, 968

Fabian A. C., Rees M. J., 1995, MNRAS, 277, L55

Fabian A. C. et al., 2000, MNRAS, 318, L65

Ford H., Tsvetanov Z., 1999, in Lecture Notes in Physics, Berlin Springer Verlag, Vol. 530, Röser H.-J., Meisenheimer K., ed, The Radio Galaxy Messier 87, p. 278

Ford H. C. et al., 1994, ApJ, 435, L27

Forman W. et al., 2007, ApJ, 665, 1057

Forman W. et al., 2005, ApJ, 635, 894

Fruscione A. et al., 2006, in Society of Photo-Optical Instrumentation Engineers (SPIE) Conference Series, Vol. 6270, Society of Photo-Optical Instrumentation Engineers (SPIE) Conference Series

Gaetz T. J., Jerius D., 2005, The HRMA User's Guide, http://cxc.harvard.edu/cal/Hrma/UsersGuide.html

Garcia M. R. et al., 2010, ApJ, 710, 755

Gaspari M., Ruszkowski M., Oh S. P., 2013, MNRAS, 432, 3401

Gebhardt K., Adams J., Richstone D., Lauer T. R., Faber S. M., Gültekin K., Murphy J., Tremaine S., 2011, ApJ, 729, 119

Genzel R., Eisenhauer F., Gillessen S., 2010, Reviews of Modern Physics, 82, 3121

Harms R. J. et al., 1994, ApJ, 435, L35

Harris D. E., Biretta J. A., Junor W., 1997, MNRAS, 284, L21

Harris D. E., Biretta J. A., Junor W., Perlman E. S., Sparks W. B., Wilson A. S., 2003, ApJ, 586, L41

Harris D. E., Cheung C. C., Biretta J. A., Sparks W. B., Junor W., Perlman E. S., Wilson A. S., 2006, ApJ, 640, 211

Harris D. E., Cheung C. C., Stawarz Ł., Biretta J. A., Perlman E. S., 2009, ApJ, 699, 305

Harris D. E. et al., 2011, ApJ, 743, 177

Hawley J. F., Balbus S. A., 2002, ApJ, 573, 738

Heckman T. M., 1981, ApJ, 250, L59

Hopkins P. F., Hernquist L., Cox T. J., Di Matteo T., Robertson B., Springel V., 2006, ApJS, 163, 1

Humphrey P. J., Buote D. A., Brighenti F., Gebhardt K., Mathews W. G., 2008, ApJ, 683, 161

Ichimaru S., 1977, ApJ, 214, 840

Igumenshchev I. V., Abramowicz M. A., 1999, MNRAS, 303, 309

Jerius D., 2002, Comparison of on-axis *Chandra* Observations of AR Lac to SAOsac Simulations, http://cxc.harvard.edu/cal/Hrma/psf/ARLac-onaxis.ps

Jerius D., Freeman M., Gaetz T., Hughes J. P., Podgorski W., 1995, in Astronomical Society of the Pacific Conference Series, Vol. 77, Shaw R. A., Payne H. E., Hayes J. J. E., ed, Astronomical Data Analysis Software and Systems IV, p. 357

Jordán A. et al., 2004, ApJ, 613, 279

Kalberla P. M. W., Burton W. B., Hartmann D., Arnal E. M., Bajaja E., Morras R., Pöppel W. G. L., 2005, A&A, 440, 775

Kirkpatrick C. C., McNamara B. R., Cavagnolo K. W., 2011, ApJ, 731, L23

Kriss G. A., Cioffi D. F., Canizares C. R., 1983, ApJ, 272, 439

Kuo C. Y. et al., 2014, ApJ, 783, L33

Li J., Ostriker J., Sunyaev R., 2013, ApJ, 767, 105

Macchetto F., Marconi A., Axon D. J., Capetti A., Sparks W., Crane P., 1997, ApJ, 489, 579

Machacek M., Nulsen P. E. J., Jones C., Forman W. R., 2006, ApJ, 648, 947

Macquart J.-P., Bower G. C., Wright M. C. H., Backer D. C., Falcke H., 2006, ApJ, 646, L111

Marrone D. P., Moran J. M., Zhao J.-H., Rao R., 2006, ApJ, 640, 308

Marrone D. P., Moran J. M., Zhao J.-H., Rao R., 2007, ApJ, 654, L57

Marshall H. L., Tennant A., Grant C. E., Hitchcock A. P., O'Dell S. L., Plucinsky P. P., 2004, in Society of Photo-Optical Instrumentation Engineers (SPIE) Conference Series, Vol. 5165, Flanagan K. A., Siegmund O. H. W., ed, X-Ray and Gamma-Ray Instrumentation for Astronomy XIII, p. 497

Matsushita K., Belsole E., Finoguenov A., Böhringer H., 2002, A&A, 386, 77

McConnell N. J., Ma C.-P., Gebhardt K., Wright S. A., Murphy J. D., Lauer T. R., Graham J. R., Richstone D. O., 2011, Nat, 480, 215

McCourt M., Sharma P., Quataert E., Parrish I. J., 2012, MNRAS, 419, 3319

McKinney J. C., Tchekhovskoy A., Blandford R. D., 2012, MNRAS, 423, 3083

McNamara B. R., Nulsen P. E. J., 2007, ARA&A, 45, 117

McNamara B. R., Rohanizadegan M., Nulsen P. E. J., 2011, ApJ, 727, 39

McNamara B. R. et al., 2000, ApJ, 534, L135

Million E. T., Werner N., Simionescu A., Allen S. W., Nulsen P. E. J., Fabian A. C., Böhringer H., Sanders J. S., 2010, MNRAS, 407, 2046

Molendi S., 2002, ApJ, 580, 815

Narayan R., Igumenshchev I. V., Abramowicz M. A., 2000, ApJ, 539, 798

Narayan R., McClintock J. E., 2008, NewA Rev., 51, 733

Narayan R., Yi I., 1994, ApJ, 428, L13

Nemmen R. S., Tchekhovskoy A., 2014, ArXiv:1406.7420

Nulsen P. E. J., 1986, MNRAS, 221, 377

Ong R. A., Mariotti M., 2010, The Astronomer's Telegram, 2542, 1

Ostriker J. P., Choi E., Ciotti L., Novak G. S., Proga D., 2010, ApJ, 722, 642

Pellegrini S., Baldi A., Fabbiano G., Kim D.-W., 2003, ApJ, 597, 175

Pellegrini S., Wang J., Fabbiano G., Kim D.-W., Brassington N. J., Gallagher J. S., Trinchieri G., Zezas A., 2012, ApJ, 758, 94

Peres C. B., Fabian A. C., Edge A. C., Allen S. W., Johnstone R. M., White D. A., 1998, MNRAS, 298, 416

Perlman E. S., Wilson A. S., 2005, ApJ, 627, 140

Peterson J. R., Fabian A. C., 2006, Phys. Rep., 427, 1

Pizzolato F., Soker N., 2005, ApJ, 632, 821

Pizzolato F., Soker N., 2010, MNRAS, 408, 961

Proga D., Begelman M. C., 2003, ApJ, 592, 767

Quataert E., Gruzinov A., 2000, ApJ, 539, 809

Quataert E., Narayan R., 2000, ApJ, 528, 236

Rafferty D. A., McNamara B. R., Nulsen P. E. J., Wise M. W., 2006, ApJ, 652, 216

Rees M. J., Begelman M. C., Blandford R. D., Phinney E. S., 1982, Nat, 295, 17

Revnivtsev M., Churazov E., Sazonov S., Forman W., Jones C., 2008, A&A, 490, 37

Reynolds C. S., Di Matteo T., Fabian A. C., Hwang U., Canizares C. R., 1996, MNRAS, 283, L111

Romanowsky A. J., Kochanek C. S., 2001, ApJ, 553, 722

Russell H. R., Fabian A. C., Sanders J. S., Johnstone R. M., Blundell K. M., Brandt W. N., Crawford C. S., 2010, MNRAS, 402, 1561

Russell H. R., McNamara B. R., Edge A. C., Hogan M. T., Main R. A., Vantyghem A. N., 2013, MNRAS, 432, 530

Russell H. R., Sanders J. S., Fabian A. C., 2008, MNRAS, 390, 1207

Salomé P., Combes F., 2008, A&A, 489, 101

Sanders J. S., Fabian A. C., 2007, MNRAS, 381, 1381

Sanders J. S., Fabian A. C., Frank K. A., Peterson J. R., Russell H. R., 2010, MNRAS, 402, 127

Sanders J. S., Fabian A. C., Sun M., Churazov E., Simionescu A., Walker S. A., Werner N., 2014, MNRAS, 439, 1182

Sharma P., McCourt M., Quataert E., Parrish I. J., 2012, MNRAS, 420, 3174

Siemiginowska A., Burke D. J., Aldcroft T. L., Worrall D. M., Allen S., Bechtold J., Clarke T., Cheung C. C., 2010, ApJ, 722, 102

Simionescu A., Werner N., Finoguenov A., Böhringer H., Brüggen M., 2008, A&A, 482, 97

Smith R. K., Brickhouse N. S., Liedahl D. A., Raymond J. C., 2001, ApJ, 556, L91

Soker N., Blanton E. L., Sarazin C. L., 2004, A&A, 422, 445

Sparks W. B., Donahue M., Jordán A., Ferrarese L., Côté P., 2004, ApJ, 607, 294

Sparks W. B., Ford H. C., Kinney A. L., 1993, ApJ, 413, 531

Stone J. M., Pringle J. E., 2001, MNRAS, 322, 461

Stone J. M., Pringle J. E., Begelman M. C., 1999, MNRAS, 310, 1002

Tan J. C., Beuther H., Walter F., Blackman E. G., 2008, ApJ, 689, 775

Tchekhovskoy A., McKinney J. C., 2012, MNRAS, 423, L55

Tchekhovskoy A., Narayan R., McKinney J. C., 2011, MNRAS, 418, L79

Tonry J. L., Dressler A., Blakeslee J. P., Ajhar E. A., Fletcher A. B., Luppino G. A., Metzger M. R., Moore C. B., 2001, ApJ, 546, 681

Tsvetanov Z. I., Hartig G. F., Ford H. C., Dopita M. A., Kriss G. A., Pei Y. C., Dressel L. L., Harms R. J., 1998, ApJ, 493, L83

Voit G. M., Donahue M., Bryan G. L., McDonald M., 2014, ArXiv e-prints

Wachter K., Leach R., Kellogg E., 1979, ApJ, 230, 274

Walsh J. L., Barth A. J., Ho L. C., Sarzi M., 2013, ApJ, 770, 86

Wang Q. D. et al., 2013, Science, 341, 981

Werner N. et al., 2010, MNRAS, 407, 2063

Wilson A. S., Yang Y., 2002, ApJ, 568, 133

Wong K.-W., Irwin J. A., Shcherbakov R. V., Yukita M., Million E. T., Bregman J. N., 2014, ApJ, 780, 9

Wong K.-W., Irwin J. A., Yukita M., Million E. T., Mathews W. G., Bregman J. N., 2011, ApJ, 736, L23

Young A. J., Wilson A. S., Mundell C. G., 2002, ApJ, 579, 560

Yuan F., Bu D.-F., 2010, MNRAS, 408, 1051

Yuan F., Quataert E., Narayan R., 2003, ApJ, 598, 301

Yuan F., Wu M., Bu D., 2012, ApJ, 761, 129